Acta Geotechnica
DOI 10.1007/s11440-006-0010-z

RESEARCH PAPER

On a viscoplastic model for rocks with mechanism-dependent characteristic times

A. F. Fossum · R. M. Brannon

Received: 31 January 2006 / Accepted: 29 April 2006

Abstract This paper summarizes the results of a theoretical and experimental program at Sandia National Laboratories aimed at identifying and modeling key physical features of rocks and rock-like materials at the laboratory scale over a broad range of strain rates. The mathematical development of a constitutive model is discussed and model predictions versus experimental data are given for a suite of laboratory tests. Concurrent pore collapse and cracking at the microscale are seen as competitive micromechanisms that give rise to the well-known macroscale phenomenon of a transition from volumetric compaction to dilatation under quasistatic triaxial compression. For high-rate loading, this competition between pore collapse and microcracking also seems to account for recently identified differences in strain-rate sensitivity between uniaxial-strain ''plate slap'' data compared to uniaxial-stress Kolsky bar data. A description is given of how this work supports ongoing efforts to develop a predictive capability in simulating deformation and failure of natural geological materials, including those that contain structural features such as joints and other spatial heterogeneities.

Keywords Plasticity · Viscoplasticity · Strain-rate sensitivity · Rock mechanics · Geomechanics · Kolsky bar · Shock loading

A. F. Fossum (✉) · R. M. Brannon
Sandia National Laboratories, P.O. Box 5800, Albuquerque, NM 87185-0751, USA
e-mail: affossu@sandia.gov

R. M. Brannon
e-mail: rmbrann@sandia.gov

1 Introduction

Simulating deformation and failure of natural geological materials (such as limestone [6], granite, soil, and frozen soil [14]) as well as rock-like engineered materials (such as concrete [18] and ceramics [1]) is at the core of a broad range of applications, including exploration and production activities for the petroleum industry, structural integrity assessment for civil engineering problems, and penetration resistance and debris field predictions for the defense community. For these materials, the common feature is the presence of microscale flaws such as porosity (which permits inelasticity even in purely hydrostatic loading) and networks of microcracks [leading to low strength in the absence of confining pressure and to noticeable nonlinear elasticity, rate-sensitivity, and differences in material behavior under triaxial extension (TXE) compared with triaxial compression (TXC)]. In addition, it is well known that strength and deformation of rock masses in situ differ considerably from strength and deformation of laboratory-scale rocks because of the presence of spatial heterogeneities found at the field scale. In this paper we focus on the laboratory scale and reserve a discussion on spatial heterogeneities for a subsequent paper.

For computational tractability and to allow relatively straightforward model parameterization using standard laboratory tests, the Sandia GeoModel [3–5, 7] strikes a balance between first-principles micromechanics and phenomenological, homogenized, and semi-empirical modeling strategies. The over-arching goal is to provide a unified general-purpose constitutive model that is predictive over a wide range of

porosities and strain rates for any geological or rock-like material.

The capability to model interacting pores and microcracks is essential in modeling observed volumetric straining during quasi-static or high strain-rate testing of Salem Limestone. However, microphysical theories often study the effect of a *single* failure mechanism, neglecting other—possibly simultaneously active—mechanisms. For example, Mohr–Coulomb theory arises from a simple criterion for microcrack growth in a non-porous matrix, whereas other theories apply only criteria for pore collapse *without* microcracking. The Sandia GeoModel unifies these and many other single-mechanism idealizations by treating their disparate response and/or limit functions essentially as basis functions, combined in a way that satisfies basic restrictions such as convexity of the limit surface. Thus, the GeoModel can handle multiple hardening and failure mechanisms, nonlinear elasticity, and nonlinear rate dependence, or (by using only a tiny subset of the 50 available control parameters) it can duplicate simpler idealized yield models such as classic von Mises plasticity and Mohr–Coulomb failure. The number of required parameters increases in *reasonable* proportion to the complexity of the material and the desired fidelity of the simulation. In the present study 22 material parameters were used, evaluated from controlled laboratory tests that will be described later in the paper.

In the remainder of this paper, we will give an overview of the mathematical formulation of the Sandia GeoModel, summarize quasi-static and high-strain-rate testing of Salem Limestone, compare model predictions with experimental data, and conclude by identifying the micromechanical processes that appear to be active during various experimental loading paths.

2 Constitutive model overview

The Sandia GeoModel is a nonlinear elastic, pressure sensitive, unified compaction/dilatation, continuous surface, strain-rate sensitive, three invariant, and mixed-hardening constitutive model for materials of any porosity and apparent strain-rate sensitivity. A Pelessone function [15] is used to model the competition between dilatation (from cracking) and compaction (from pore collapse), and thus the GeoModel shares some features with earlier work by Schwer and Murry [16]. For stress paths that result in brittle deformation, failure is associated ultimately with the attainment of a peak stress and subsequent work-softening. Even when all principal stresses are compressive, tensile or extensile microcrack growth can result in macroscopically dilatational (volume increasing) strains. At higher pressures, however, these processes can simultaneously undergo strain-hardening deformation associated with macroscopically compactive volumetric strain (e.g., pore collapse).

The source of inelastic deformation in geological materials (or in rock-like materials such as concrete and ceramics) is primarily growth and coalescence of microcracks and pores. Under massive confining pressures, inelasticity could include plasticity in its traditional dislocation sense or, more generally, might result from other microphysical mechanics, (internal locking, phase transformation, twinning, etc.). The GeoModel predicts observed material response without explicitly addressing how the material behaves as it does, and thus it reflects subscale inelastic phenomena *en ensemble* by phenomenologically matching standard test data to interpolation functions (of course, no parameter adjustments are allowed in validation testing). The GeoModel makes no explicit reference to microscale properties such as porosity, grain size, or crack density. Instead, the overall combined effects of the microstructure are modeled by casting the macroscale theory in terms of macroscale variables that are realistic to measure in the laboratory. Considerations guiding the structure of the GeoModel's macroscale response functions are (1) consistency with microscale theory, (2) consistency with macroscale constraints, (3) computational tractability, (4) suitability to capture trends in characterization data, and (5) physics-based judgments about how a material should behave in application domains where controlled experimental data cannot be obtained.

The GeoModel presumes that there exists a convex contiguous elastic domain of stress levels for which the material response can be considered elastic. The boundary of this elastic domain is called the yield surface. Aside from supporting kinematic hardening, the GeoModel is isotropic, which means that the criterion for the onset of plasticity depends only on the three principal values of the stress tensor, (σ_1, σ_2, σ_3), but not on the principal directions. Consequently, as illustrated in Fig. 1, the yield surface may be visualized as a surface embedded in a 3D space where the axes are the principal stresses. The elastic domain is the interior of this surface.

Whereas the yield surface is the boundary of elastically obtainable stress states, the *limit* surface is the boundary of stresses that are quasi-statically obtainable by *any* means, elastic or plastic. Points

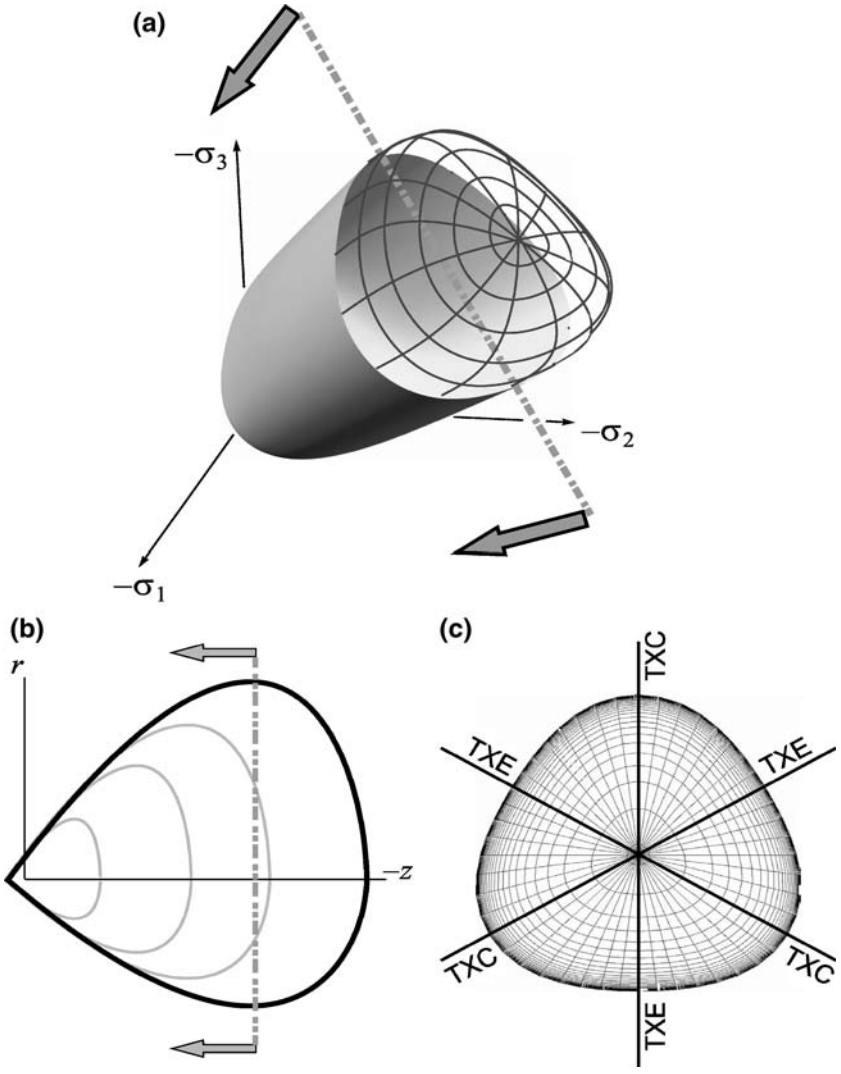

Fig. 1 GeoModel continuous yield surface (**a**) three-dimensional view in principal stress space with the high pressure ''cap'' shown as a wire frame, (**b**) the meridional ''side'' view with the cap shown on the more compressive right-hand side of the plot, and (**c**) the octahedral view, which corresponds to looking down the hydrostat showing triaxial extension (*TXE*) and triaxial compression (*TXC*) stress states

outside a yield surface might be attainable through a hardening process, but points outside the limit surface are not attainable by any quasi-static process. Points on the limit surface mark the onset of material softening. Consequently, a state on the limit surface is attainable at least once, but might not be attainable thereafter. This paper reports only the equations governing material response up to the limit state. To simulate subsequent softening, additional equations (not described here) must be applied because softening usually induces a change in type of the partial differential equations for momentum balance, requiring a response from the host code to alter its solution algorithm. Before the onset of material softening, the limit surface may be regarded as fixed. Because the limit surface contains all attainable stress states, it follows that the set of all possible yield surfaces is contained within the limit surface as shown in Fig. 2.

3 Mathematical foundations

The GeoModel is founded upon an additive decomposition of the strain rate $\dot{\boldsymbol{\varepsilon}}$ into separate contributors, $\dot{\boldsymbol{\varepsilon}}^{\mathbf{e}}$ from elastic straining and $\dot{\boldsymbol{\varepsilon}}^{\mathbf{p}}$ from inelastic straining:

$$\dot{\boldsymbol{\varepsilon}} = \dot{\boldsymbol{\varepsilon}}^{\mathbf{e}} + \dot{\boldsymbol{\varepsilon}}^{\mathbf{p}} \tag{1}$$

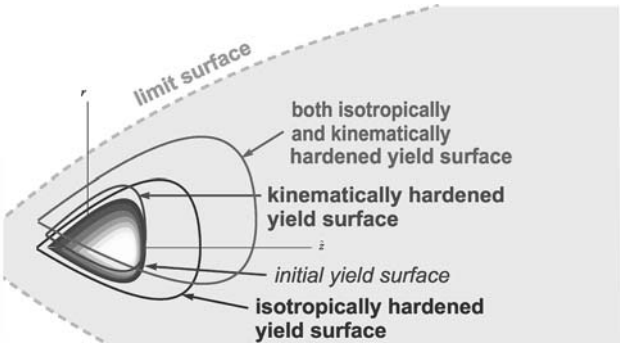

Fig. 2 Distinction between a yield surface and a limit surface. This sketch shows meridional profiles of yield surfaces that might evolve from the initial surface. All achievable stress states, and thus all possible yield surfaces are contained within the limit surface

Strictly speaking, the GeoModel permits the host code to employ any definition of the strain so long as it is conjugate to the stress $\boldsymbol{\sigma}$ in the sense that the work rate per unit reference volume is given by

$$\dot{W} = \boldsymbol{\sigma} : \dot{\boldsymbol{\varepsilon}} \tag{2}$$

Here, all references to the stress $\boldsymbol{\sigma}$ and the strain rate $\dot{\boldsymbol{\varepsilon}}$ must be understood to be cast in the unrotated frame, which automatically satisfies the principle of material frame indifference and lends itself well to computations because the transformations to/from the material frame may be implemented in the form of an unobtrusive code wrapper. To date, all implementations of the GeoModel have approximated the strain rate by the unrotated symmetric part of the velocity gradient:

$$\dot{\boldsymbol{\varepsilon}} = \frac{1}{2}\mathbf{R}^{\mathrm{T}} \cdot (\nabla \mathbf{v} + \mathbf{v}\nabla) \cdot \mathbf{R} \tag{3}$$

where $\mathbf{v}$ is the velocity vector and tensor $\mathbf{R}$ is the rotation from the polar decomposition of the deformation gradient. The conjugate stress is the unrotated Cauchy stress.

The strain rate in Eq. 3 is an approximation because, for general deformations, it is not precisely equal to the rate of any proper function of the deformation. The approximate strain rate exactly equals the unrotated logarithmic (Hencky) strain rate for any deformation having stationary principal stretch directions. It is an excellent approximation to the Hencky strain rate even when principal stretch directions change orientation as long as the shear strains remain small (volumetric strains may be arbitrarily large). For geological applications, material rupture generally occurs well before shear strains become large, so Eq. 3 is a prudent choice for the strain rate measure.

3.1 Elasticity

The GeoModel supports linear or nonlinear hypoelasticity. The stress is governed by a rate form of Hooke's law,

$$\dot{\boldsymbol{\sigma}} = \mathbf{C} : \dot{\boldsymbol{\varepsilon}}^{\mathrm{e}} \tag{4}$$

The elastic stiffness tensor $\mathbf{C}$ is presumed to be isotropic. Hence, Eq. 4 may be written as two separate and much simpler equations, one for the volumetric response and the other for the deviatoric response:

$$\dot{\bar{p}} = K\dot{\bar{\varepsilon}}_{\mathrm{v}}^{\mathrm{e}} \tag{5}$$

and

$$\dot{\mathbf{S}} = 2G\dot{\boldsymbol{\gamma}}^{\mathbf{e}} \tag{6}$$

where $\dot{\bar{p}}$ is the rate of pressure (negative of the mean stress), K is the tangent bulk modulus, $\dot{\bar{\varepsilon}}_{\mathrm{v}}^{\mathrm{e}}$ is the volumetric elastic strain rate (trace of $\dot{\boldsymbol{\varepsilon}}^{\mathrm{e}}$), $\dot{\mathbf{S}}$ is the rate of the stress deviator, G is the tangent shear modulus, and $\dot{\boldsymbol{\gamma}}^{\mathbf{e}}$ is the deviatoric part of the elastic strain rate. The GeoModel algorithm employs the mechanics convention that stress and strain are positive in tension. Above and in what follows, we use an overbar to denote the negative of a variable. This convention was used, for example, in our equation for the pressure–volume response because the mean stress p is typically compressive (negative) in most applications of the GeoModel and therefore $\bar{p}$ and $\bar{\varepsilon}_{\mathrm{v}}^{\mathrm{e}}$ are typically positive. Of course, Eq. 5 remains valid for volumetric expansion ($\bar{\varepsilon}_{\mathrm{v}}^{\mathrm{e}} < 0$) and tensile mean stresses ($\bar{p} < 0$) as well.

The GeoModel includes nonlinear elasticity by permitting the elastic tangent moduli to vary with the stress according to the following interpolation functions (designed to be well suited to most geological materials):

$$K = b_0 + b_1 \exp\left(-\frac{b_2}{|I_1|}\right) \tag{7}$$

$$G = g_0 \left[\frac{1 - g_1 \exp\left(-g_2 J_2^{1/2}\right)}{1 - g_1}\right] \tag{8}$$

where I_1 is the first invariant of the Cauchy stress; J_2 is the second invariant of the deviatoric stress tensor; and b_k, g_k are material parameters.

3.2 Limit surface

Whereas a yield surface encloses *elastically* obtainable stress states, the limit surface in Fig. 2 is the boundary of stress states attainable by *any* quasistatic means (elastic or inelastic). While a yield surface can evolve, the limit surface is fixed in stress space. Whereas a yield surface can exhibit deformation-induced anisotropy, the limit surface for an initially isotropic material must be itself isotropic. Experimentally, the limit surface is determined by noting the values of the stress invariants at the peak state (i.e., at the onset of softening) for a variety of loading paths.

In mechanics, a standard invariant triplet is

$$I_1 = \operatorname{tr}\boldsymbol{\sigma}, \quad J_2 = \frac{1}{2}\operatorname{tr}\mathbf{S}^2, \quad J_3 = \frac{1}{3}\operatorname{tr}\mathbf{S}^3 \tag{9}$$

where $\mathbf{S}$ is the stress deviator. The GeoModel also employs the Lode triplet $(r, \bar{\theta}, \bar{z})$, comprising cylindrical coordinates in principal stress space centered about the hydrostat:

$$r = \sqrt{2J_2}, \quad \sin(3\bar{\theta}) = -\frac{J_3}{2}\left(\frac{3}{J_2}\right)^{3/2} \quad \bar{z} = \frac{-I_1}{\sqrt{3}} \tag{10}$$

As here defined, the Lode angle $\bar{\theta}$ is –30° in TXC, zero in pure shear, and +30° in TXE.

For an initially isotropic material, the limit surface, defined by $F(\boldsymbol{\sigma}) = 0$, must also be isotropic and may therefore be written in the following general form:

$$F(\boldsymbol{\sigma}) = J_2(\boldsymbol{\sigma}) - \frac{F_f^2[I_1(\boldsymbol{\sigma})]}{\Gamma^2\left[\bar{\theta}(\boldsymbol{\sigma}), I_1(\boldsymbol{\sigma})\right]} \tag{11}$$

As explained below, the function F_f characterizes pressure variation in peak shear strength in TXC. The function Γ, which simply equals 1 in Drucker–Prager theory, allows modeling the tendency for geological materials to have a lower strength in TXE than in TXC.

The TXC Limit Function, F_f: Based on observed trends in TXC failure data for rocks, the limit function F_f is taken to be an affine-exponential spline:

$$F_f(\bar{I}_1) = \left[a_1 - a_3\exp\left(-a_2\bar{I}_1\right)\right] + a_4\bar{I}_1 \tag{12}$$

The user-specified a_k parameters are determined from experimental data. Specifically, the $(I_1, \sqrt{J_2})$ data pairs to be fitted to Eq. 12 are found by conducting TXC experiments at various lateral confining pressures, recording the values of I_1 and $\sqrt{J_2}$ at the moment when $\sqrt{J_2}$ reaches its peak (i.e., at the onset of softening).

Optionally, Eq. 12 reduces to classical idealized failure theories by appropriate choices for the parameters (e.g., only a_1 is needed for von Mises or Tresca theory, while a_4 is also nonzero for linear Drucker–Prager or Mohr–Coulomb theory). The ability to reduce to simpler models is essential for code verification against analytical solutions.

The Lode-angle function, $\Gamma\left(\bar{\theta}, I_1\right)$: The shape of the octahedral limit profile is controlled by the Lode-angle function, $\Gamma\left(\bar{\theta}, I_1\right)$, which is determined *in part* by user-specification of the ratio, $\Psi(\bar{I}_1)$, of strengths in TXE $(\mathrm{TXE}, \bar{\theta} = -30°)$ and TXC $(\mathrm{TXC}, \bar{\theta} = 30°)$. The strength ratio is found by conducting TXE experiments at a variety of lateral confining pressures to obtain a TXE strength curve similar to $F_f(I_1)$ for TXC. Then Ψ is the ratio of the ordinates of the TXE and TXC limit curves.

If TXE data are unavailable, the user may optionally instruct the GeoModel to estimate Ψ by coupling it to the slope of the TXC meridional limit function according to

$$\Psi(\bar{I}_1) = \frac{1}{1 + \sqrt{3}A(\bar{I}_1)} \text{ where } A(\bar{I}_1) \equiv \left(\frac{\partial\sqrt{J_2}}{\partial\bar{I}_1}\right)_{\bar{\theta}=30°} \tag{13}$$

This formula, which generalizes similar coupling in Mohr–Coulomb theory, not only estimates Ψ, but also is a simple way to include pressure-dependence of the strength ratio, allowing the octahedral profile to transition smoothly from a triangle at low pressures to a circle at high pressures.

Henceforth, dependence of $\Gamma\left(\bar{\theta}, I_1\right)$ on $\bar{I}_1$ will be implicit in $\Psi(\bar{I}_1)$. From Eq. 11, note that Γ is inversely proportional to $\sqrt{J_2}$. Hence, $\Gamma\left(\bar{\theta}\right)$ must range from $1/\Psi$ to 1 as the Lode angle varies from $\bar{\theta} = -30°$ in TXE to $\bar{\theta} = 30°$ in TXC. Convexity of the octahedral profile requires $1/2 < \Psi < 1$ and

$$\Gamma''\left(\bar{\theta}\right) + \Gamma\left(\bar{\theta}\right) \geqslant 0 \tag{14}$$

Three Lode-angle interpolation functions (see Fig. 3) are supported in the GeoModel:

1. Gudehus [10]:

$$\Gamma\left(\bar{\theta}\right) = \frac{1}{2}\left[1 + \sin\left(3\bar{\theta}\right) + \frac{1}{\Psi}\left[1 - \sin\left(3\bar{\theta}\right)\right]\right]$$

2. Willam–Warnke [19]:

$$\Gamma(\bar{\theta}) = \frac{4(1-\Psi^2)\cos^2(\alpha^*) + (2\Psi-1)^2}{2(1-\Psi^2)\cos(\alpha^*) + (2\Psi-1)\sqrt{4(1-\Psi^2)\cos^2(\alpha^*) + 5\Psi^2 - 4\Psi}}$$

where $\alpha^* = \pi/6 + \bar{\theta}$

3. Mohr–Coulomb [17]:

$$\Gamma(\bar{\theta}) = \frac{2\sqrt{3}}{3-\sin\phi}\left(\cos\bar{\theta} - \frac{\sin\phi\sin\bar{\theta}}{\sqrt{3}}\right)$$

$$\sin\phi = 3\frac{(1-\Psi)}{1+\Psi}$$

The Gudehus and Willam–Warnke options are fully differentiable, whereas the Mohr–Coulomb option has a vertex at triaxial states. For the Gudehus case, the convexity requirement, Eq. 14, requires $7/9<\Psi<9/7$. When $\Psi = 1$, the Mohr–Coulomb option simplifies to the Tresca hexagon, and the other two options simplify to the von Mises (or Drucker–Prager) circle.

3.3 Yield surface

In this work, the term ''plasticity'' is broadened to include not only the usual flow of material by dislocations, but also any other mechanisms that lead to a marked departure from elasticity. Examples include crack growth, pore collapse, or perhaps even phase transition. Whereas the previously discussed limit function $F(\boldsymbol{\sigma})$ characterizes peak stress states attainable by any quasistatic means (elastic or plastic), a *yield function* $f(\boldsymbol{\sigma}, \cdots)$ marks the boundary of *elastically obtainable* stress states, and it depends on more than just stress so that it may evolve in response to plastic loading. Whereas points outside the limit surface can never be reached, points outside a yield surface (but inside the limit surface) may be reached through a hardening evolution process corresponding to irreversible changes of the material's microstructure. Rather than explicitly tracking each of these microscale failure mechanisms explicitly, the ''yield'' surface itself characterizes them all in an ensemble phenomenological manner by using internal state variables.

By definition, the set of all possible yield surfaces must be contained within the limit surface (see Fig. 2). The yield surface is expected to inherit some features from the limit surface, especially at low pressures where very little plastic hardening precedes softening. For rocks and rock-like materials, the yield surface has a shape similar to the one illustrated in Fig. 1. Figure 1b shows a ''side'' meridional profile of the yield surface, and a family of other profiles from which the yield surface might have evolved over time. Note from Fig. 1b that very little of the yield surface exists in the tensile domain, implying that materials of this type are very weak in tension. Unlike the limit surface, the yield surface for geological materials has a so-called cap (''cage'' in Fig. 1) that admits inelasticity—usually attributed to pore collapse—even in purely hydrostatic compression. As pores are crushed out, the yield surface evolves, pushing the cap (see Fig. 1b) outward so that ever-increasing pressure is required to continue pore collapse. As explained below, this type of yield surface evolution is accommodated via isotropic hardening using an internal state variable κ that evolves toward infinity as porosity goes to zero.

Though infrequently applied (often for lack of data), deformation-induced anisotropy (the Bauschinger effect) is modeled via conventional kinematic hardening wherein the symmetry axis of the yield surface can shift in stress space. In this case, the invariants appearing in the isotropic yield function are those of the *shifted* stress tensor, defined by

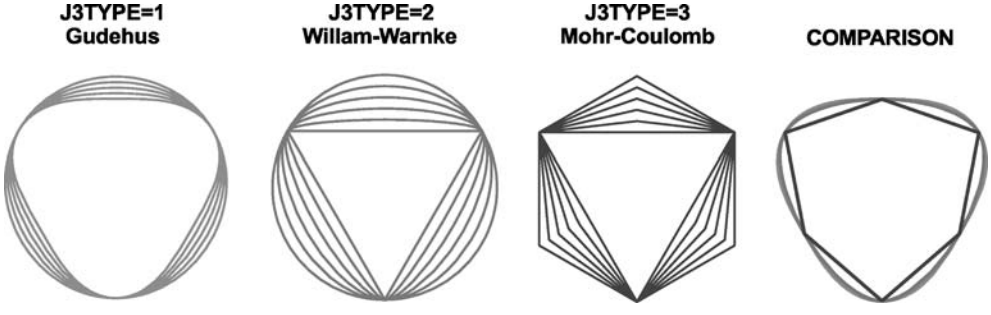

Fig. 3 Octahedral yield profiles, plotted at allowable values of the strength ratio. (The comparison is made for a strength ratio of $\Psi = 0.8$)

$$\boldsymbol{\xi} = \mathbf{S} - \boldsymbol{\alpha} \tag{15}$$

Here, the backstress $\boldsymbol{\alpha}$ is a deviatoric tensor-valued internal state that defines the origin about which the yield surface is centered. As the backstress tensor changes (according to an evolution equation described later), the yield surface translates in stress space in a direction perpendicular to the hydrostat. The GeoModel is otherwise fully isotropic, both elastically and plastically, implying that its yield function can be cast in terms of invariants of the shifted stress:

$$f = f\left(I_1, J_2^{\xi}, J_3^{\xi}; \kappa\right) \tag{16}$$

where κ is the compaction internal state variable (discussed below) and

$$I_1 = \operatorname{tr}\boldsymbol{\sigma} \quad J_2^{\xi} = \frac{1}{2}\operatorname{tr}\boldsymbol{\xi}^2 \quad J_3^{\xi} = \frac{1}{3}\operatorname{tr}\boldsymbol{\xi}^3 \tag{17}$$

When kinematic hardening is active, the Lode invariants in Eq. 10 are redefined in terms of the shifted stress:

$$r = \sqrt{2J_2^{\xi}}, \quad \sin(3\bar{\theta}) = -\frac{J_3^{\xi}}{2}\left(\frac{3}{J_2^{\xi}}\right)^{3/2}, \quad \bar{z} = \frac{-I_1}{\sqrt{3}} \tag{18}$$

Each yield surface corresponding to various values of κ and $\boldsymbol{\alpha}$ is, as indicated in Fig. 2, bounded by the shear limit surface $F_f = 0$. Therefore, the yield function is expected to share some qualitative features with the shear limit function in Eq. 11, while additionally depending on internal variables. Specifically,

GeoModel yield function:

$$f(\boldsymbol{\sigma}, \boldsymbol{\alpha}, \kappa) = J_2^{\xi}\Gamma^2\left(\bar{\theta}\right) - \left[F_f(I_1) - N\right]^2 F_c^2(I_1, \kappa) \tag{19}$$

The yield *criterion* results when f=0. Elastic states correspond to $f < 0$. Recall that the function F_f represents the ultimate limit on the amount of shear the material can support in the absence of pores. The material parameter N characterizes the maximum allowed translation of the yield surface. If kinematic hardening is disabled (i.e., if N is specified to be zero), then the backstress is zero, making J_2^{ξ} simply the second invariant of the stress deviator. By appearing as a multiple of F_f, the compaction function F_c produces the ''cage'' in Fig. 1, accommodating material weakening caused by porosity. The compaction function F_c is normalized to transition smoothly from 0 at the hydrostatic elastic limit to 1 at low pressures. Thus, at low pressures, where F_c typically equals 1.0, the shape of the meridional yield profile in Fig. 1b is inherited primarily from the limit function F_f. As long as F_c is continuously differentiable, the yield strength continuously transitions into the compaction domain at high pressures where pore collapse begins to compete with microcracking as a significant mechanism for failure (see Fig. 4). The shape of the octahedral yield profile, which is determined by $\Gamma\left(\bar{\theta}\right)$, is inherited from that of the limit surface, but its size will be smaller in the compaction domain where $F_c < 1$.

Whereas *single points* (the peaks) are easily taken from each TXC test to determine the limit function F_f, the remainder of the data leading up to that peak must be used in a far more difficult model calibration effort to determine not only the onset of inelasticity, but also the hardening evolution of the strength. The initial elastic limit is reached at a value of $\sqrt{J_2}$ that is lower than the peak strength F_f by some amount N, reduced perhaps by a compaction function F_c if the material initially contains pores. As is true for any plasticity model that employs more than one internal state variable, sorting out the individual contributions of each damage mechanism is a matter of identifying loading paths that suppress evolution of all but one internal variable at a time and/or optimizing undetermined parameters to best match a suite of standard laboratory calibration tests. If a calibrated set of parameters fails to adequately match subsequent validation data, then one must conclude that the model itself (not its parameters) must be enhanced to incorporate additional or improved physics.

Flow rule: The direction of the plastic strain rate is expressed in the form

$$\dot{\boldsymbol{\varepsilon}}^{\mathrm{p}} = \dot{\lambda}\left(\frac{\partial \phi}{\partial \boldsymbol{\sigma}}\right)_{\boldsymbol{\alpha},\kappa} \tag{20}$$

where $\phi(\boldsymbol{\sigma}, \boldsymbol{\alpha}, \kappa)$ is a flow potential function and $\dot{\lambda}$ is a multiplier called the consistency parameter, determined by requiring the stress to remain on the yield surface during inelastic loading. The subscripts on the partial derivative indicate that the internal state

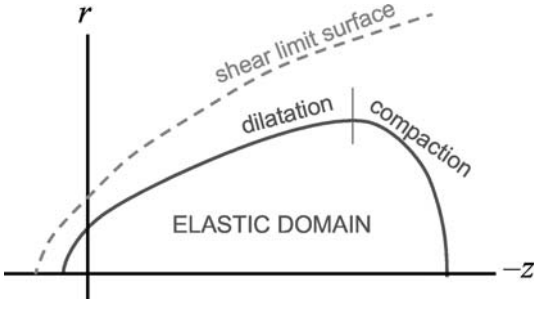

Fig. 4 Compaction and dilatation dominant regions in the meridional plane

variables are held constant. In mathematical structure, the flow potential is the same as the yield function f, but with different values for constant material parameters. Unless specifically directed to apply non-associativity, the GeoModel defaults the flow parameters to equal their counterparts in the yield function.

Following conventional plasticity theory, the two internal state variables, κ and $\boldsymbol{\alpha}$, are presumed to evolve in proportion to the consistency parameter $\dot{\lambda}$. These evolution equations are discussed below, along with further details on the structure of the yield function.

3.3.1 Compaction function, F_c, and the evolution function for κ

Referring to Eq. 19, the compaction function F_c accounts for the presence of pores in a material by controlling where the yield function will intersect the $\bar{I}_1$ axis in compression and by degrading the material shear strength near this critical hydrostatic elastic limit. This behavior is achieved in the GeoModel by a compaction function of the form

$$F_c^2(I_1;\kappa) = \begin{cases} 1 & \text{if} \quad \bar{I}_1 < \bar{\kappa} \\ 1 - \left(\frac{\bar{I}_1 - \bar{\kappa}}{\bar{X} - \bar{\kappa}}\right)^2 & \text{otherwise} \end{cases} \tag{21}$$

Here $\bar{\kappa}$ is an internal state variable marking the point where F_c branches (smoothly) from a constant value of 1 at low pressure to begin its descent along an elliptical path to the value 0 at the hydrostatic compression elastic limit where the yield surface crosses the hydrostat at $\bar{I}_1 = \bar{X}$.

For compaction-dominated loading, evolution of $\bar{X}$ can be inferred from its relationship with volumetric plastic strain observed in hydrostatic compression. The data from such ''crush curve'' testing are fitted to an affine-exponential spline:

$$\begin{aligned} \bar{\varepsilon}_{\mathrm{v}}^{\mathrm{p}} &= p_3\left[1 - \exp\left\{-\left(p_1 + p_2\bar{\xi}\right)\bar{\xi}\right\}\right] \\ \bar{\xi} &= \bar{X} - \bar{p}_0 \end{aligned} \tag{22}$$

where $\bar{\varepsilon}_{\mathrm{v}}^{\mathrm{p}}$ is the plastic volumetric strain and the p_k are fitting constants. Although the GeoModel makes no explicit reference to microscale quantities, the plastic volumetric strain may be loosely interpreted as the change in porosity induced by plastic strain. Accordingly, p_3 approximately equals the initial porosity, and $\bar{p}_0$ is the value of $\bar{I}_1$ at the *initial* hydrostatic elastic limit (note: $\bar{X}$ is the *evolving* hydrostatic elastic limit).

Evolution equations for $\bar{\kappa}$ and $\bar{X}$ are guided by microphysical theories for the influence of porosity on shear strength, which suggest that pore collapse causes the cap to translate along the hydrostat without significantly changing curvature. For pressure-sensitive materials, this notion is applied by co-evolving $\bar{\kappa}$ and $\bar{X}$ such that the ratio $(\bar{X} - \bar{\kappa})/F_f(\bar{\kappa})$ remains fixed at a user-specified constant R, called the ''shape parameter''. Thus, the evolution of $\bar{X}$ determined from Eq. 22 also controls the evolution of $\bar{\kappa}$ in the compaction domain. Guided by trends in observed data and by microphysical theories, the evolution of $\bar{\kappa}$ changes character in the dilatation domain where crack opening not only produces volumetric expansion, but also induces damage that quickly ushers the stress state toward the softening limit. This consideration of the competition between pores and cracks has motivated the following evolution equation for $\kappa(= -\bar{\kappa})$

$$\dot{\kappa} = h_\kappa \dot{\lambda} \tag{23}$$

where the isotropic hardening modulus is

$$h_\kappa = \min \left\{ \begin{array}{l} 3\dfrac{\partial \phi}{\partial I_1}\left(\dfrac{\mathrm{d}X/\mathrm{d}\bar{\varepsilon}_{\mathrm{v}}^{\mathrm{p}}}{1 - RF_f'(\kappa)}\right), \\ \dfrac{(I_1 - \kappa)}{R}\left(\dfrac{\mathrm{d}X/\mathrm{d}\bar{\varepsilon}_{\mathrm{v}}^{\mathrm{p}}}{1 - RF_f'(\kappa)}\right) \end{array} \right\} \tag{24}$$

and $F_f'(\kappa)$ is the first derivative of $F_f(I_1)$ with respect to I_1 evaluated at κ. As a reminder, R is the shape parameter; ϕ is the plastic flow potential; X represents the intersection of the compaction function F_c with the I_1 axis; and the derivative $\mathrm{d}X/\mathrm{d}\bar{\varepsilon}_{\mathrm{v}}^{\mathrm{p}}$ is determined from Eq. 22. The first branch of Eq. 24 applies when the stress state falls on the ''compaction dominated'' part of the yield surface in Fig. 4. The second branch, which dominates in the dilatation regime, is phenomenological based on observed behavior of geological materials undergoing shear-enhanced dilatation in TXC loading.

3.3.2 Kinematic hardening evolution law

Kinematic hardening entails using a shifted stress tensor $\boldsymbol{\xi} = \mathbf{S} - \boldsymbol{\alpha}$ instead of the actual stress to define the origin for the yield function. Initially, the backstress is zero. Since the yield function itself is defined in terms of $F_f(I_1) - N$ (i.e., the distance between the *limit* surface and the initial *yield* surface) the maximum kinematic translation that can occur before reaching the limit surface equals the user-specified offset parameter N. In other words, the following function decays from 1 to 0 as the limit surface is approached:

$$G^{\alpha}(\boldsymbol{\alpha}) = 1 - \frac{\sqrt{J_2^{\alpha}}}{N}, \text{ where } J_2^{\alpha} = \frac{1}{2}\mathrm{tr}\,\boldsymbol{\alpha}^2 \tag{25}$$

Upon the onset of yielding the backstress evolves in proportion to the deviatoric part of the plastic strain rate according to

$$\dot{\boldsymbol{\alpha}} = HG^{\alpha}(\boldsymbol{\alpha})\dot{\boldsymbol{\gamma}}^{\mathrm{p}} \tag{26}$$

where H is a user-specified constant and

$$\dot{\boldsymbol{\gamma}}^{\mathrm{p}} = \mathrm{dev}\dot{\boldsymbol{\varepsilon}}^{\mathrm{p}} = \mathrm{dev}\left(\dot{\lambda}\frac{\partial \phi}{\partial \boldsymbol{\sigma}}\right) \tag{27}$$

Combining the above equations with Eq. 20, the backstress $\boldsymbol{\alpha}$ is evolved according to

$$\dot{\boldsymbol{\alpha}} = \mathbf{H}_{\boldsymbol{\alpha}}\dot{\lambda} \tag{28}$$

where

$$\mathbf{H}_{\alpha} = HG^{\alpha}(\boldsymbol{\alpha})\mathrm{dev}\left(\frac{\partial \phi}{\partial \boldsymbol{\sigma}}\right) \tag{29}$$

3.4 Elastic–plastic coupling

A cap model is used when the material being studied contains enough porosity (or highly compliant second phase inclusions) so that inelastic volume reduction becomes possible through irreversible reduction of pore space. Intuitively, one might expect the elastic moduli to stiffen as pores collapse, but the material might actually become more elastically compliant as shown in Fig. 5 (a phenomenon that might be explained, for example, by rubblization of a ligament network).

Regardless of its microphysical origins, the elastic moduli of a porous material are permitted to vary with plastic strain by generalizing the nonlinear elastic moduli expressions in Eqs. 7 and 8 to

$$K = b_0 + b_1\exp\left(-\frac{b_2}{|I_1|}\right) - b_3\exp\left(-\frac{b_4}{|\bar{\varepsilon}_{\mathrm{v}}^{\mathrm{p}}|}\right) \tag{30}$$

$$G = g_0\left[\frac{1 - g_1\exp\left(-g_2 J_2^{1/2}\right)}{1 - g_1}\right] - g_3\exp\left(-\frac{g_4}{\gamma_{\mathrm{equiv}}^{\mathrm{p}}}\right) \tag{31}$$

where $\gamma_{\mathrm{equiv}}^{\mathrm{p}}$ is the equivalent plastic shear strain (which, for proportional loading, is conjugate to the equivalent shear stress, $\sqrt{J_2}$), and $\bar{\varepsilon}_{\mathrm{v}}^{\mathrm{p}}$ is the plastic compaction volume strain. Specifically,

$$\gamma_{\mathrm{equiv}}^{\mathrm{p}} = \int \sqrt{2}\|\dot{\boldsymbol{\gamma}}^{\mathrm{p}}\|\mathrm{d}t \text{ and } \bar{\varepsilon}_{\mathrm{v}}^{\mathrm{p}} = \int \mathrm{tr}(\dot{\boldsymbol{\varepsilon}}^{\mathrm{p}})\mathrm{d}t \tag{32}$$

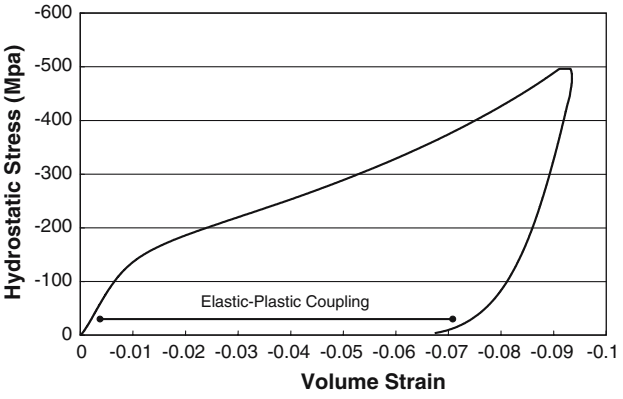

Fig. 5 Elastic–plastic coupling: deformation-induced changes in elastic moduli

4 Rate dependence

Under high strain rates, elastic material response occurs almost instantaneously, but the physical mechanisms that give rise to observable inelasticity cannot proceed instantaneously. Materials have inherent ''viscosity'' that retards the rate at which damage accumulates. For example, cracks grow and pores collapse at a finite speed. Consequently, the quasi-static solution for material damage will not be realized unless sufficient time elapses to permit the cracks and pores to change size. As the internal state variables (which phenomenologically represent the microscale material state such as porosity and crack density) evolve towards their quasi-static solution, the stress will also approach the quasi-static solution. Until sufficient time has elapsed for this process to occur, the stress state may lie outside the yield surface or possibly even outside the limit surface. If the applied strain is released during this damage accumulation period, the total damage will be lower than it would have been under quasi-static loading through the same strain path.

The GeoModel uses a generalized Duvaut–Lions [2] rate-sensitive formulation, illustrated qualitatively in Fig. 6. Consider a loading increment Δt during which the strain increment is prescribed to be $\Delta\boldsymbol{\varepsilon}$. Two limiting solutions for the updated stress can be readily

computed: (1) the low-rate (quasistatic) solution $\boldsymbol{\sigma}^{\mathbf{L}}$ that is found by solving the rate-independent GeoModel equations described previously and (2) the high-rate solution $\boldsymbol{\sigma}^{\mathbf{H}}$ corresponding to insufficient time for any plastic response to develop so that it is simply the trial elastic stress. As illustrated in Fig. 6, the Duvaut–Lions rate formulation is based on a viscoplastic differential equation, the solution of which shows that the updated stress will be (approximately) a linear interpolation between the low-rate quasistatic plasticity solution $\boldsymbol{\sigma}^{\mathbf{L}}$ and the high-rate purely elastic solution $\boldsymbol{\sigma}^{\mathbf{H}}$. In other words, there exists a scalar between 0 and 1 that depends on the strain rate such that

$$\boldsymbol{\sigma} \approx \boldsymbol{\sigma}^{\mathbf{L}} + \eta\left(\boldsymbol{\sigma}^{\mathbf{H}} - \boldsymbol{\sigma}^{\mathbf{L}}\right) \tag{33}$$

The update for internal state variables is structured similarly, but uses a somewhat different weighting factor. For a given strain increment, the interpolation factor η varies from 1 at high strain rates (when Δt is small) to 0 at low strain rates (when Δt is large), as illustrated in the graph inset of Fig. 6, where the abscissa is normalized by a factor τ called the material's "characteristic response time."

The Duvaut–Lions equations are the following:

$$\begin{aligned}
&\dot{\boldsymbol{\varepsilon}} = \dot{\boldsymbol{\varepsilon}}^{\mathrm{e}} + \dot{\boldsymbol{\varepsilon}}^{\mathrm{vp}} \\
&\dot{\boldsymbol{\sigma}} = \mathbf{C}^{\mathrm{e}} : \dot{\boldsymbol{\varepsilon}}^{\mathrm{e}} = \mathbf{C}^{\mathrm{e}} : \left(\dot{\boldsymbol{\varepsilon}} - \dot{\boldsymbol{\varepsilon}}^{\mathrm{vp}}\right) \\
&\dot{\boldsymbol{\varepsilon}}^{\mathrm{vp}} = \frac{1}{\tau}\left(\mathbf{C}^{\mathrm{e}}\right)^{-1} : \left(\boldsymbol{\sigma} - \boldsymbol{\sigma}^{\mathrm{low}}\right) \\
&\dot{\boldsymbol{\sigma}} + \frac{1}{\tau}\boldsymbol{\sigma} = \mathbf{C}^{\mathrm{e}} : \dot{\boldsymbol{\varepsilon}} + \frac{1}{\tau}\boldsymbol{\sigma}^{\mathrm{low}} \\
&\dot{\boldsymbol{\alpha}} + \frac{1}{\tau}\boldsymbol{\alpha} = \frac{1}{\tau}\boldsymbol{\alpha}^{\mathrm{low}} \\
&\dot{\kappa} + \frac{1}{\tau}\kappa = \frac{1}{\tau}\kappa^{\mathrm{low}}
\end{aligned} \tag{34}$$

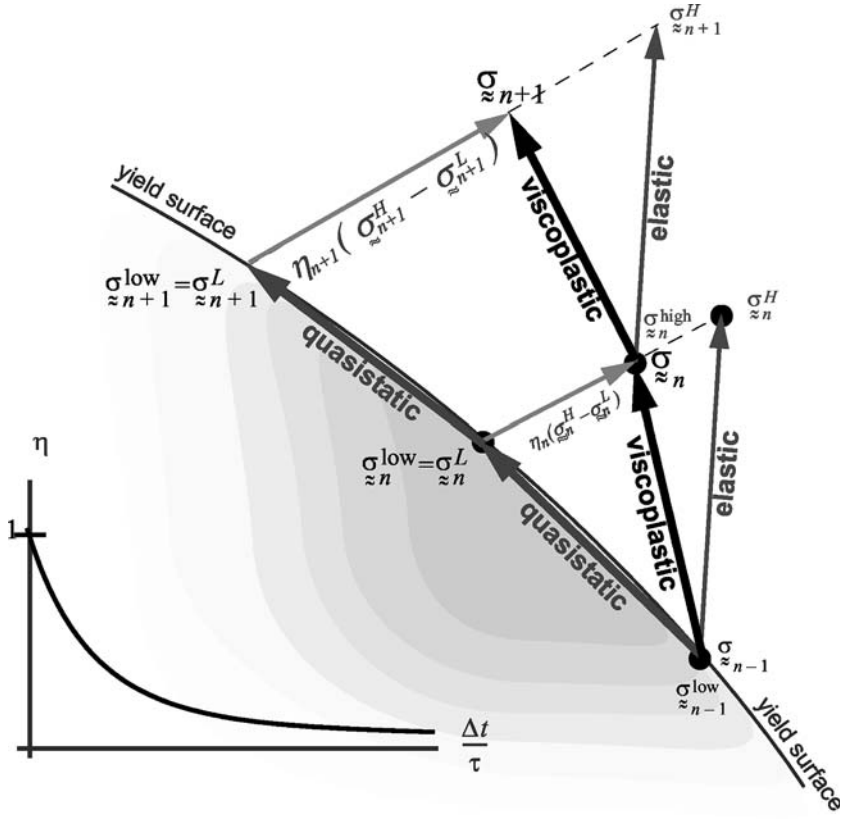

Fig. 6 *Rate dependence*. For a given strain increment, two limiting solutions can be readily found. The "low rate" solution $\boldsymbol{\sigma}^{\mathbf{L}}$, which lies on the yield surface, is the solution to the rate independent GeoModel governing equations. The high rate solution $\boldsymbol{\sigma}^{\mathbf{H}}$ is simply the trial elastic stress. The actual updated rate-dependent viscoplastic stress σ falls between these two limiting case solutions so that $\boldsymbol{\sigma} = \boldsymbol{\sigma}^{\mathbf{L}} + \eta\left(\boldsymbol{\sigma}^{\mathbf{H}} - \boldsymbol{\sigma}^{\mathbf{L}}\right)$. The *inset graph* shows how the scale factor η varies with the loading interval. If the loading interval is long relative to the material's characteristic response time τ, then sufficient time exists to develop plastic response fully and the updated solution therefore coincides with the quasi-static solution $\boldsymbol{\sigma}^{\mathbf{L}}$. If the loading interval is considerably shorter than the material's characteristic response time, then the solution will be the high-rate elastic solution

where ''low'' denotes time-varying quasi-static solution; ''vp'' denotes ''visco-plastic''; and η is the viscosity coefficient.

The characteristic time, which was determined empirically to provide flexibility in matching high strain-rate data for a wide range of rock types, is given by

$$\tau = \begin{cases} f\left(\dot{\varepsilon}^{\text{equiv}}\right) = T_1\left(\frac{1}{\tau_{\text{ref}}\dot{\varepsilon}^{\text{equiv}}}\right)^{T_2} & \text{for } \bar{\varepsilon}_{\text{v}}^{\text{p}} \le 0 \\ T_4 f\left(\dot{\varepsilon}^{\text{equiv}}\right)\left[1 + \langle T_5(T_3 - I_1)\rangle^2\right] & \text{for } \bar{\varepsilon}_{\text{v}}^{\text{p}} > 0 \end{cases} \quad (35)$$

where the T_{k} are constants, τ_{ref} is a reference characteristic time.

5 Comparison of model versus experiment

5.1 Quasi-static results

The GeoModel was fitted to Salem Limestone data obtained from standard quasi-static laboratory experiments including TXC, TXE, hydrostatic compression, and uniaxial strain. Comparisons of the GeoModel against experimental data will now be shown. A single set of parameters was used for all of the simulations.

Figure 7 compares the GeoModel predictions with measured results for hydrostatic compression and uniaxial strain tests.

Figure 8 shows the GeoModel's fit to experimental TXC and TXE limit-states. It was found that the

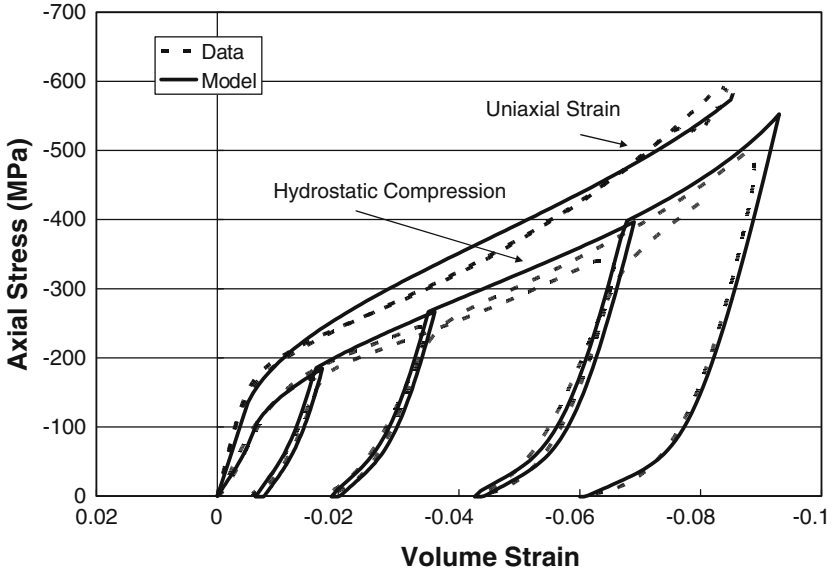

Fig. 7 GeoModel fit versus measured data

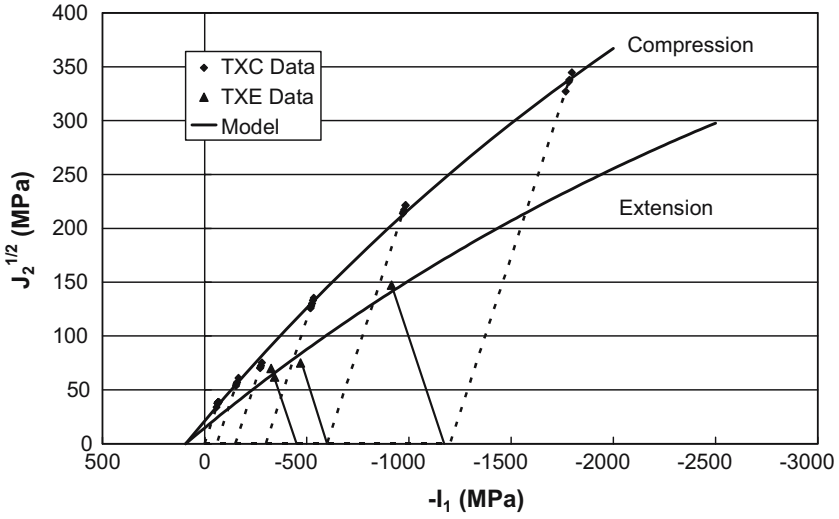

Fig. 8 GeoModel prediction versus measured triaxial compression and triaxial extension limit states

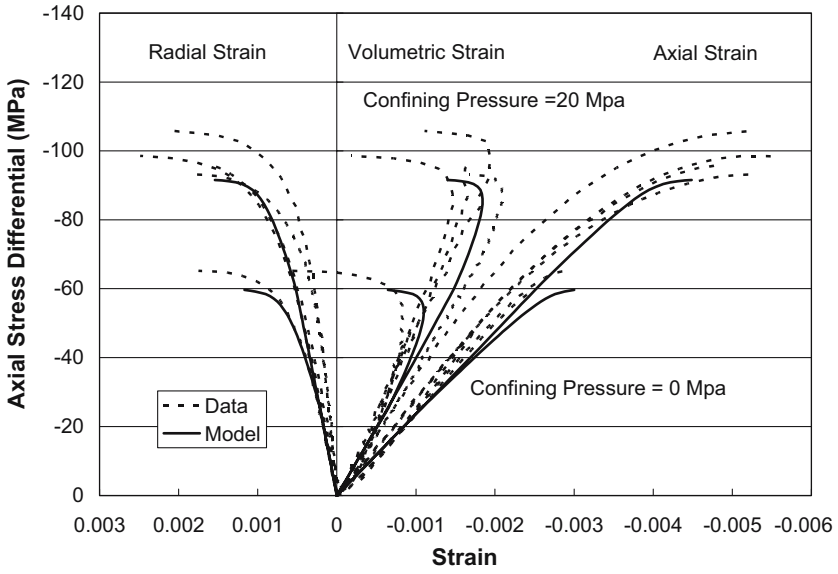

Fig. 9 GeoModel prediction versus measured results for an unconfined compression test and a triaxial compression test conducted at 20 MPa

triaxial extensile strength is approximately 70% of the triaxial compressive strength [i.e., Ψ in Eq. 13 equals 0.7].

Figure 9 shows the GeoModel prediction of an unconfined compression test and a TXC test conducted at 20 MPa confining pressure. The model accurately captures the initial compaction caused by pore collapse and then smoothly transitions to dilatational deformation.

Figure 10 shows the GeoModel prediction versus measured results for a TXC test conducted at 400 MPa lateral confining pressure. The model accurately reflects the micromechanical processes that occur during the loading process, including the simultaneous competition between (compactive) pore collapse and (dilatational) microcrack growth. Figure 10 shows the sequence of yield envelopes that evolve to keep up with the linear stress trajectory in stress space. The indicated points in stress space are cross-referenced to corresponding points on the axial stress versus volume strain curve recorded during the test. The line labeled ''A'' in Fig. 10 corresponds to the hydrostatic elastic limit. The line labeled ''B'' corresponds to the change in loading from hydrostatic compression to triaxial compression. The line labeled ''D'' corresponds to the transition from compaction to dilatation (see Fig. 4). Thus, as the pore space becomes depleted, the dilatational mechanisms begin to dominate. The line labeled ''C'' corresponds to the point at which softening initiates.

5.2 Dynamic results

Parameters for the rate-sensitive part of the model were determined from unconfined [8] and confined [9] Kolsky bar (Split Hopkinson Pressure Bar) tests. The following results illustrate the importance of the deformation mechanisms on the apparent strain-rate sensitivity of Salem Limestone. Under impulsive fracture conditions, brittle materials have been shown to exhibit much higher fracture resistance than they do under quasi-static loading conditions. At the macroscopic scale this process is modeled phenomenologically through a rate dependence model for which ''characteristic response time'' (τ in Fig. 6 and Eq. 35) must be inferred from macroscale experimental data. At the microscale, this rate dependence likely stems from local stress perturbations, inertial effects, and friction. It will be shown for Salem Limestone that the characteristic time for compaction-dominated deformation is approximately three times greater than that for dilatation-dominated behavior, which suggests (not too surprisingly) that different inelasticity mechanisms—in this case pore collapse and micro-cracking—require different amounts of time to develop fully.

A Kolsky bar apparatus [11, 12] is used to determine the peak stress in an axial stress–strain experiment in compression at several different constant axial strain rates with hydrostatic confinement [9] and without hydrostatic confinement [8]. A conventional

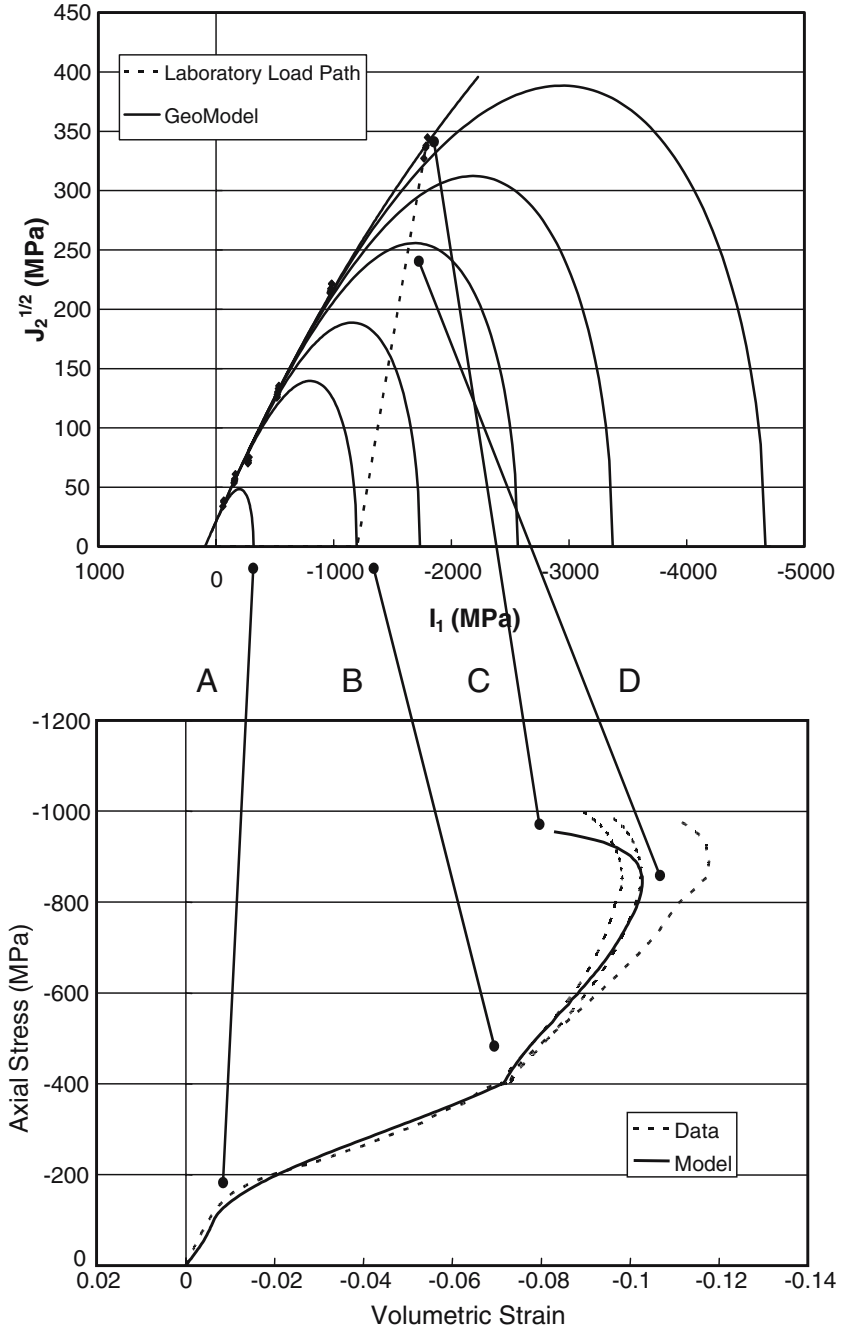

Fig. 10 This figure shows the load path followed during a triaxial compression test, the evolving yield surface, and points on the evolving yield surface that correspond to different points on the volumetric stress–strain curve

Kolsky bar comprises a striker bar, an incident bar, a transmission bar, and a specimen placed between the incident and transmission bars. The striker bar is launched at the incident bar from a gas gun to cause an elastic compression wave to travel in the incident bar toward the specimen. If the impedance of the specimen is less than that of the bars, an elastic tensile wave is reflected into the incident bar and an elastic compression wave is transmitted into the transmission bar. Frew et al. [8] place a thin copper disk on the impact surface of the incident bar (a pulse shaper) to produce a non-dispersive ramp pulse that propagates in the incident bar to produce uniform dynamic stress equilibrium and a nearly constant strain rate in the specimen. For the confined Kolsky bar experiments, pressure vessels are used to impose a nearly constant hydrostatic pressure on the specimen before the striker bar is launched [9].

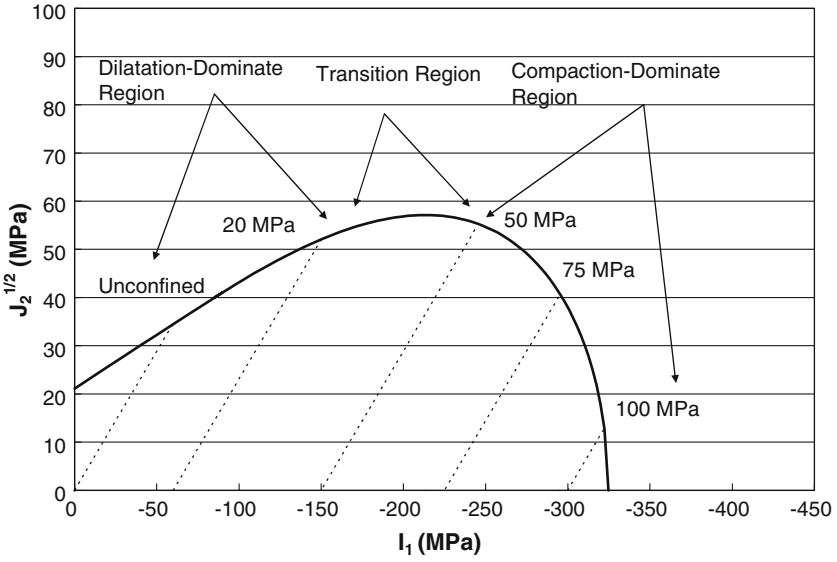

Fig. 11 Load paths followed for the unconfined and confined Kolsky-bar dynamic experiments

The straight lines in Fig. 11 are the load paths in stress space followed during the dynamic tests. The curved line is the initial yield surface that was predetermined from separate (quasistatic) calibration data. Note that the load paths for the unconfined case and the 20 MPa confining pressure case ($I_1 = -60$ MPa) intersect the initial yield surface on the dilatation-dominant side of the yield surface. The other load paths, in which the specimens are loaded initially to 50, 75, and 100 MPa, intersect the initial yield surface on the compaction-dominant side of the yield surface. For the unconfined and 20 MPa-confined experiments, there is little or no pore collapse during the test. For the remaining experiments pore collapse is the dominant deformation mechanism.

To model these dynamic tests it is necessary to include one characteristic response time for (dilatation-dominated) micro-cracking but a different one for (compaction-dominated) pore collapse. Equation 35 allows a transition to be made in the characteristic response time when there is a change in the predominant deformation mechanism during loading. Figure 12 illustrates the need for a transition that depends on the nature of the loading. In this figure, peak stress is plotted versus confining pressure for Kolsky-bar experiments conducted at strain rates of approximately

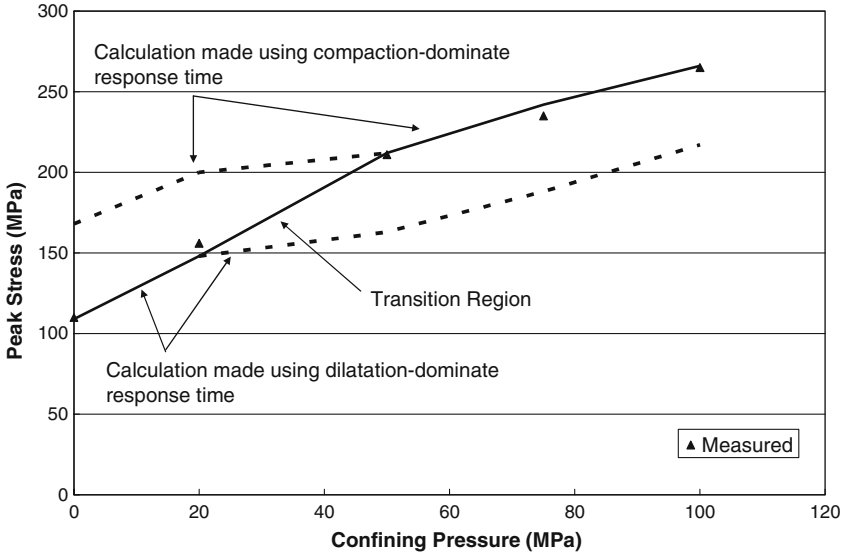

Fig. 12 Comparisons against data of peak stress versus confining pressure for calculations made with the characteristic response time for dilation-dominated responses and the characteristic response time for compaction-dominated responses

100 s^{-1}. If the characteristic response time for a dilatation-dominated mechanism is used to model all of the experiments, the calculated peak stresses for the compaction-dominated cases are severely under-estimated. On the other hand if the characteristic response time for a compaction-dominated mechanism is used to model all of the experiments, the calculated peak stresses for the dilatation-dominated cases are severely over estimated. The transition region shown in Fig. 12 corresponds to the transition region in the yield surface shown in Figs. 11 and 4. This is the locus on the yield surface where the inelastic volumetric compaction strain-rates equal the inelastic volumetric dilatation strain-rates resulting in a nearly constant-volume process. These results suggest that the characteristic response time for the compaction-dominated deformation of Salem Limestone is approximately three times greater than the value of the characteristic response time for dilatation-dominated deformation.

As a validation test, all of the parameters determined to this point (see Table 1) are used to predict the plate-slap, plane shock-wave experiments of Larson and Anderson [13] on Salem Limestone that provide uniaxial-strain data at extremely high strain rates on the order of 10^5–10^7 s^{-1}. Figure 13 shows the results for uniaxial strain simulations made at strain rates of 10^5, 10^6, 10^7, and 10^{-5} s^{-1} (the experimental quasi-static uniaxial-strain results conducted at 10^{-5} s^{-1} are included for comparison). As seen by a visual inspection of the figure, the Hugoniot data fall within the simulations corresponding to the experimental strain rates reported in [13]. It is concluded therefore that the model with the parameter estimates given in Table 1 gives an acceptable representation for experiments conducted on Salem Limestone over a strain-rate range that includes 12 orders of magnitude, (10^{-5}–10^7 s^{-1}). The stress space path for uniaxial-strain loading is shown in Fig. 14. In that simulation, the initial yield surface is first reached near the compaction-dominated side of the yield surface and continues even further into the compaction regime with continued straining. Thus the characteristic time used in these simulations is the one determined from the confined Kolsky bar experiments, which is three times the characteristic time determined from the unconfined Kolsky bar experiments.

Table 1 Material parameter set for the Sandia GeoModel

b_0 (Pa)	b_1 (Pa)	b_2 (Pa)	b_3 (Pa)	b_4 (–)	g_0 (Pa)
1.30E10	4.25E10	4.11E8	1.2E10	0.021	9.86E9
g_1 (–)	g_2 (Pa^{-1})	g_3 (Pa)	g_4 (–)	a_1 (Pa)	a_2 (Pa^{-1})
0.0	0.0	0.0	0.0	8.43E8	2.73E-10
a_3 (Pa)	a_4 (–)	p_0 (Pa)	p_1 (Pa^{-1})	p_2 (Pa^{-2})	p_3 (–)
8.22E8	1.00E-10	3.14E8	1.22E-10	1.28E-18	0.084
R (–)	Ψ(–)	N (Pa)	H (Pa)	T_1 (s)	T_2 (–)
6	0.72	1.2E7	1.0E11	4.0E-4	0.835
T_3 (Pa)	T_4 (–)	T_5 (Pa^{-2})	τ_{ref} (s)		
0	3	0	1		

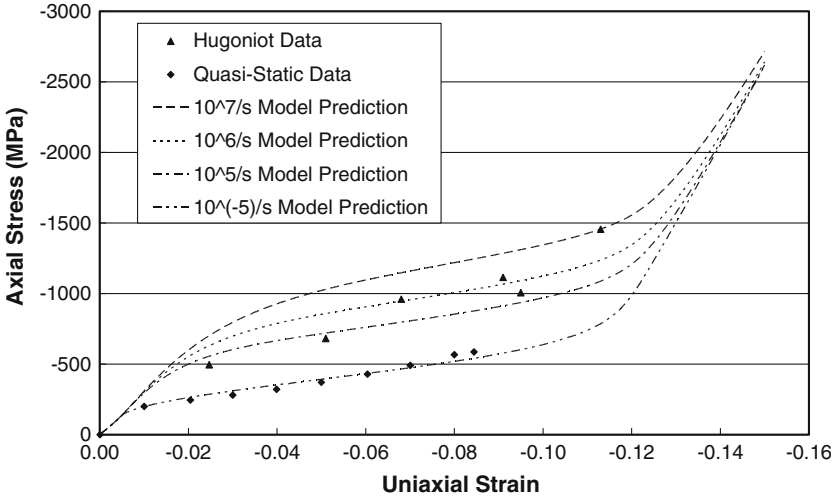

Fig. 13 Measured versus predicted uniaxial strain responses for quasi-static and shock-wave experiments

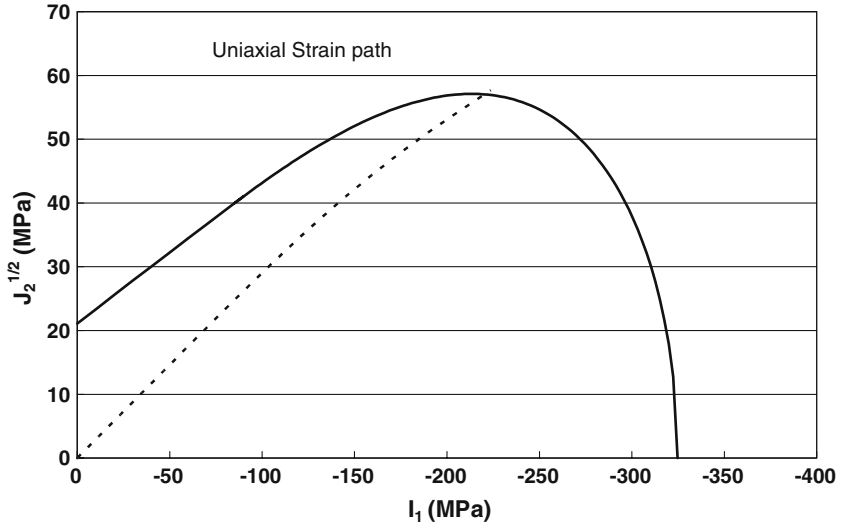

Fig. 14 Uniaxial-strain load path in meridional stress space

6 Discussion

In impact fracture situations, such as those found in the unconfined and confined Kolsky bar experiments, a stress level can be transiently achieved that is considerably greater than the stress level required to initiate growth of the most severe flaw. An additional period of time (often called ''incubation time'') may elapse before actual fracture. As macroscopic straining proceeds, the stress on the specimen can continue to increase. During this time, the critical stress level required to produce crack growth can occur at many other flaws in the material. For high-rate loading conditions, therefore, crack growth can be initiated at very many flaws.

As the overall straining continues, the flaws begin to grow in the form of microcracks and the stress continues to rise. Eventually the increasing stress rate corresponding to a constant strain rate decreases because the effective stiffness of the sample diminishes. The stress rate becomes zero at some time, and thereafter the stress level falls with continued straining. Ultimately, the growing microcracks coalesce into one or more macroscopic cracks. On average, coalescence occurs when each growing microcrack extends to a length equal to the initial spacing of activated flaws. The impact strength at constant strain rate is the maximum stress acting on the specimen during this process.

The situation becomes more complicated when the material contains a homogeneously distributed number of pores. As the pores begin to collapse during loading, the grains adjacent to pores tend to rotate and slide relative to one-another giving rise to perturbations in the local stress fields of activated flaws, which may become deactivated. With continued deformation at constant strain rate, the de-activated flaws may become re-activated and/or different flaws, i.e., flaws that were not activated before pore collapse, may become activated during pore collapse. The result of this process is that there is an additional incubation time that contributes to the time it takes to produce a macroscopic failure. In the case of Salem Limestone this time is approximately three times greater than the time it takes to produce a macroscopic failure when no pore collapse occurs.

If the constant axial strain rate in a confined Kolsky-bar test could be maintained for a sufficient duration, the load path followed in the test would pass through the transition region as the yield surface expands isotropically as shown in Figs. 10 and 11. We hypothesize, therefore, that because the characteristic response times are different in the compaction-dominant and dilatation-dominant regions, the stress–strain response would reflect this transition as shown in Fig. 15, which was simulated using the characteristic response time given by Eq. 35. Validating this unconfirmed prediction in the laboratory will require test system enhancements, such as longer incident and transmission bars.

7 Summary

The mathematical structure has been given for a general-purpose rock and soil plasticity model. It was

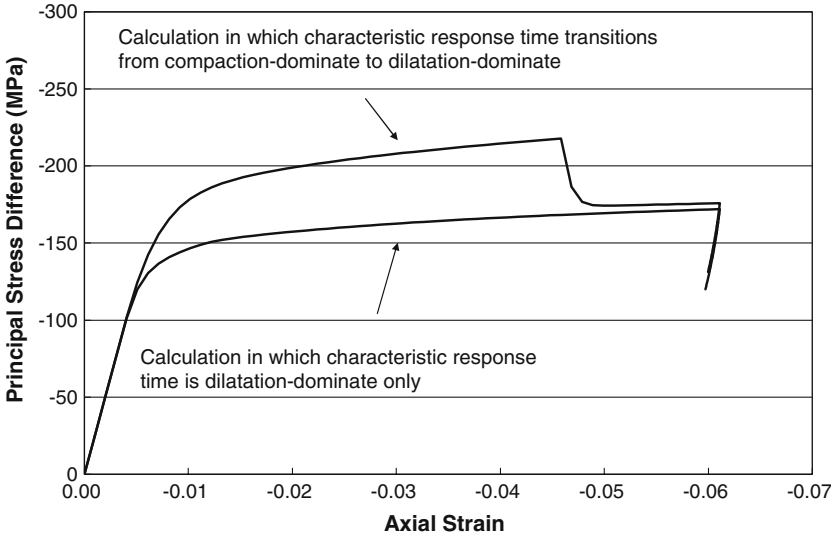

Fig. 15 Confined Kolsky-bar simulation showing a transition from compaction-dominated deformation to dilatation-dominated deformation

shown that two deformation mechanisms, microcracking and pore collapse, act concurrently and competitively, depending on the load path. A realistic representation of observed experimental behavior requires that they be modeled simultaneously using a continuously differentiable yield and limit surface. Comparisons were given of model predictions versus experimental measurements for a suite of quasi-static tests and for dynamic tests conducted at strain rates ranging from 10^{-5}–10^{7} s^{-1}. It was observed that the characteristic time for compaction-dominated deformation is approximately three times greater than the characteristic time for microcrack-dominated deformation for Salem Limestone.

The development of the Sandia GeoModel, which has been based on observations made on the laboratory scale, forms the core of a larger effort aimed at developing a predictive capability for natural geologic materials on the field scale. On this larger scale, structural features, rock joints, and other spatial heterogeneities are incorporated into the model resulting in strengths and stiffnesses that are much lower than the strengths and stiffnesses observed in the laboratory. Moreover, aleatory uncertainty and size effects in material strength have been incorporated to extend the model into the softening domain. A summary of these efforts will be presented in a forthcoming paper.

Acknowledgements The authors gratefully acknowledge the support of the Advanced Simulation and Computing Physics and Engineering Models Program entitled, ''Enhancement Geomechanics Modeling,'' led by John Pott of Sandia National Laboratories. Sandia National Laboratories is a multiprogram laboratory operated by Sandia Corporation, a Lockheed Martin Company, for the United States Department of Energy under Contract DE-A04-94AL85000.

References

1. Arguello JG, Fossum AF, Zeuch DH, Ewsuk KG (2001) Continuum-based FEM modeling of alumina powder compaction. KONA 19:166–177
2. Duvaut G, Lions JL (1972) Les inequations en mecanique et en physique. Dunod, Paris
3. Fossum AF, Brannon RM (2004) The Sandia GeoModel: theory and user's guide. Technical report No SAND2004-3226 UC-405, Sandia National Laboratories, Albuquerque
4. Fossum AF, Brannon RM (2004) Unified compaction/dilatation, strain-rate sensitive, constitutive model for rock mechanics structural analysis applications. In: Proceedings of the 6th North America rock mechanics symposium: rock mechanics across borders and disciplines, Houston, in CD-ROM
5. Fossum AF, Fredrich JT (2000) Cap plasticity models and compactive and dilatant pre-failure deformation. In: Girard J, Liebman M, Breeds C, Doe T (eds) Pacific rocks 2000: rock around the rim. A.A. Balkema, Amsterdam, pp 1169–1176
6. Fossum AF, Senseny PE, Pfeifle TW, Mellegard KD (1994) Experimental determination of probability distributions for parameters of a Salem limestone cap plasticity model. Mech Mat 21:119–137
7. Foster CD, Regueiro RA, Fossum AF, Borja RI (2005) Implicit numerical integration of a three-invariant, isotropic/kinematic hardening cap plasticity model for geomaterials. Comp Meth Appl Mech Eng 194:5109–5138
8. Frew DJ, Forrestal MJ, Chen W (2001) A split Hopkinson pressure bar technique to determine compressive stress–strain data for rock materials. Exp Mech 41:40–46
9. Frew DJ, Forrestal MJ, Akers SA (2006) A triaxial Hopkinson pressure bar technique to determine compressive stress–strain data for rock materials. (in press)
10. Gudehus G (1973) Elastoplastische stoffgleichungen fur Trockenen sand. Ingenieur Arch 42:151–169

11. Kolsky H (1949) An Investigation of the mechanical properties of materials at very high rates of loading. Proc R Soc Lond B 62:676–700
12. Kolsky H (1963) Stress waves in solids. Dover, New York
13. Larson DB, Anderson GD (1979) Plane shock wave studies of porous geologic media. J Geophys Res 84:4592–4600
14. Lee MY, Fossum AF, Costin LS, Bronowski D (2002) Frozen soil material testing and constitutive modeling. Technical report No SAND2002-0524, Sandia National Laboratories, Albuquerque
15. Pelessone D (1989) A modified formulation of the cap model. Technical report No GA-C19579, Gulf Atomics
16. Schwer LE, Murry YD (1994) A three-invariant smooth cap model with mixed hardening. Int J Num Anal Meth Geomech 18:657–688
17. Senseny PE, Fossum AF, Pfeifle TW (1983) Non-associative constitutive laws for low porosity rocks. Int J Num Anal Meth Geomech 7:101–115
18. Warren TL, Fossum AF, Frew DJ (2004) Penetration into low strength (23 MPa) concrete: target characterization and simulations. Int J Impact Eng 30:477–503
19. Willam KG, Warnke EP (1975) Constitutive model for the triaxial behavior of concrete. In: Concrete structures subjected to triaxial stresses. ISMES, Bergamo